RESEARCH ARTICLE - SOLID EARTH SCIENCES

Preliminary horizontal co-seismic displacements caused by the 2023 Mw 7.8 and Mw 7.5 Türkiye earthquakes estimated using high-rate GPS observations

Shengtao Feng[1,2,3] · Li Jie[1,2,4] · Li Guirong[1,2,4] · Li Rui[1,2,4] · Sulitan Yusan[1,2,4] · Aerdake Kadeerbieke[1]

Abstract

Using high-rate (1 Hz) global positioning system (GPS) data, coseismic displacement estimates are obtained for the 2023 Mw 7.8 Pazarcik and Elbistan Mw 7.5 Türkiye earthquakes. The estimated largest displacements caused by the Mw 7.8 event are observed at station *ante* with an eastward component displacement of 31cm and at station *mly1* with a southward component displacement of 39cm. The displacements caused by the Mw 7.8 Pazarcik event show left-lateral displacements along the nodal plane, which is consistent with the focal mechanism. The largest displacements caused by the Mw 7.5 event are a westward component displacement of 450 cm and a northward component displacement of 97cm at the station *ekz1* which is only 6 km from the epicenter of the event. Based on high-rate GPS time series, the surface wave propagation of the Mw 7.8 Elbistan earthquake is preliminarily estimated at an overall speed of approximately 2.9 km/s, with a slightly higher speed of 3.1 km/s along the northeast direction and 3.0 km/s along the east direction. High-rate GPS measurements show a prominent advantage of temporal resolution for earthquake sequences with short intervals, and preliminary displacement estimates could be made with only a few hours of observations. The displacement estimation provides constraints for the inversion of the rupture process and seismic source mechanisms.

Keywords High-rate GPS · Coseismic displacement · Propagation speed of surface response

Introduction

The 2023 February 6 Mw 7.8 Pazarcik Türkiye earthquake caused severe damage to a large area, followed by the Mw 7.5 Elbistan earthquake within 10 hours and with a distance of less than 100 km. The interferometric synthetic aperture radar measurements provide rupture distribution of the earthquake sequence (Reitman et al. 2023). However, the spatiotemporal closeness makes it difficult to distinguish the coseismic deformation caused by each event. Daily GPS observations with a sampling interval of 30 seconds provide effective constraints for velocity, deformation, slip distribution and other kinematic information of crustal movements (Abdrakhmatov et al. 1996; Li et al. 2012; Jiang et al. 2014; Goudarzi et al. 2016; Zhan 2021; Li et al. 2022, Wu et al. 2022), but they are limited in rapid coseismic displacement estimations due to temporal resolution. High-rate GPS measurements show a prominent advantage in temporal resolution for earthquake sequences with short intervals (Ge et al. 2000; Larson et al. 2003; Elósegui et al. 2006; Larson 2009; Avallone et al. 2012; Clotaire Michel et al. 2017; Guo et al. 2021; Li et al. 2023). High-rate GPS data are used for rapid determination of earthquake magnitude, centroid moment tensor determination and rupture evolution to provide earthquake or tsunami early warning and disaster prevention (Blewitt et al. 2006; Melgar et al. 2012; Goldberg et al.

Edited by Prof. Maria Marsella (ASSOCIATE EDITOR) / Prof. Ramon Zuñiga (CO-EDITOR-IN-CHIEF).

✉ Li Jie
  lijiexj@sohu.com

  Shengtao Feng
  fengshengtao@sina.com

1 Xinjiang Pamir Intracontinental Subduction National Observation and Research Station, Ürümqi, China

2 Earthquake Agency of Xinjiang Uygur Autonomous Region, Ürümqi, China

3 First Monitoring and Application Center, China Earthquake Administration, Tianjin, China

4 Urumqi Institute of Central Asia Earthquake, China Earthquake Administration, Ürümqi, China

2018). In this article, preliminary coseismic displacement estimates for the Mw 7.8 and Mw 7.5 events are obtained using high-rate (1 Hz) GPS data provided by Türkiye Ulusal Sabit GNSS Ağı (tusaga-aktif.gov.tr) and the international GNSS service (IGS) through the Crustal Dynamics Data Information System (CDDIS) (Noll 2010). Further inversion of the rupture process and source mechanism can be made based on the displacement estimates (Yokota et al 2009; Yue et al. 2011; Xu et al. 2021; Zhijie Jia et al. 2022). Sub-daily process of slow slip events can also be inverted from high-rate GPS observations (Itoh Yuji et al. 2022). The GPS time series with complete records are used to estimate the propagation speed of the surface wave radiated by the earthquake. For stations closest to the epicenters of the two events which stopped recording data shortly after the events and reactivated later, observations before and after each event are used to estimate coseismic displacements. Together with continuous coseismic observations, the results provide preliminary constraints for ground deformation field and rupture process inversion. The GPS stations used in this article are shown in Figure 1. Also shown are the active faults in the vicinity (Seyitoğlu et al. 2022), the focal mechanism from the Global Centroid-Moment-Tensor (CMT) Project (Ekström et al. 2012) and the tectonic setting in the inset map.
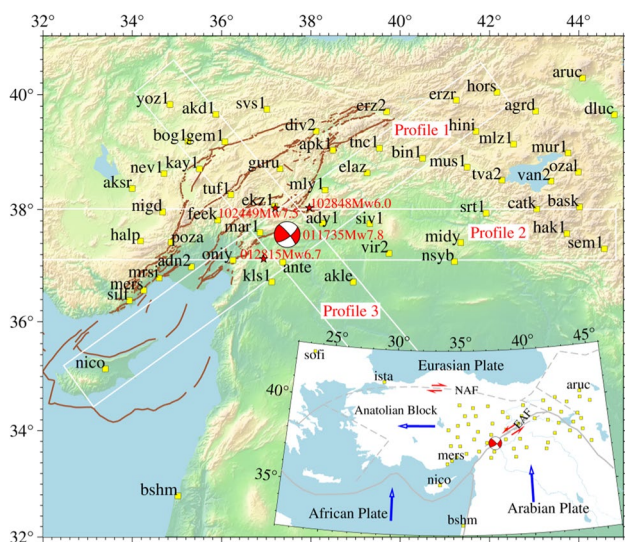

Fig. 1 Distribution of GPS stations (stations annotated in the inset map are IGS stations) and sketch of tectonic setting in the area (inset map). Yellow squares denote GPS stations. The focal mechanism of the Mw 7.8 earthquake is denoted with the red beachball. Three other earthquakes include Mw 6.7, Mw 7.5, and Mw 6.0 on February 6, 2023 are denoted with red asterisks. White rectangles denote profiles for surface wave speed analysis. NAF is the abbreviation for North Anatolian Fault and EAF is for East Anatolian Fault. Plate boundary is plotted with grey solid lines. Block boundary is plotted with grey dashed lines. The relative motions of major tectonic structures are qualitatively denoted with blue arrows in the inset map

The African and Arabian plates move northward and converge with the Eurasian plate, which causes the westward motion of the Anatolian block (Dan McKenzie 1972; Barka 1997). The Anatolian block rotates counter-clockwise while escaping from the collision between the Eurasian plate and the Arabian plate and the motion occurs mainly on the North Anatolian Fault and East Anatolian Fault (Barka 1997; Bulut et al. 2012). Along the North Anatolian Fault, the right-lateral strike-slip accommodates most of the westward motion of the Anatolian block, while the left-lateral strike-slip motion mainly occurs along the East Anatolian Fault. Seismicity in this area is usually related to the tectonic movements of the three first-order plates (the Eurasian plate, the African plate and the Arabian plate) and the smaller tectonic block (the Anatolian block).

The earthquake sequence including 4 Mw≥6.0 earthquakes (Fig. 1) occurred on the boundary between the Arabian plate and the Anatolian block. The Anatolian block moves southwestward relative to the Arabian plate with left-lateral strike-slip motion mainly occurring along the East Anatolian fault (denoted as EAF in Fig. 1) (Emre 2018). In this article, we describe the method used to process high-rate GPS data in the region. Position time series of near-field sites are plotted with indications of coseismic movements to verify the results. Then, the time series of all sites recording distinguishable coseismic movements are used to estimate the propagation speed of the surface waves. To preliminarily estimate coseismic displacements at each site, linear fitting is then used to analyze the position time series of the sites. An eastward component displacement of 31cm at site *ante* and a southward component displacement of 39cm at site *mly1* are estimated to be the largest displacements caused by the Mw 7.8 event. The displacements show left-lateral movement along the nodal plane, which is consistent with the focal mechanism. A westward component displacement of 450cm and a northward component displacement of 97cm at the site *ekz1* are the largest displacements caused by the Mw 7.5 event. Using high-rate GPS position time series, the surface wave propagation speed caused by the Mw 7.8 Elbistan earthquake is preliminarily estimated at an overall speed of approximately 2.9 km/s.

Data processing

The TRACK module of GAMIT/GLOBK software is used to process the high-rate GPS data (Herring et al. 2003). Data from 46 local GPS stations and 6 IGS stations are processed (Fig. 1 and Appendix Tab. 1). The high-rate GPS data are concatenated to one-hour sessions of GPS time 00, 01, 02, 03, and 10, 11, 12, 13, and 14 on February 6. List of observations of the first 4 sessions is shown in appendix Table 1, IGS stations are labeled with asterisks. Firstly, the IGS sites

sofi and *ista* are used to estimate the far field effects of the Mw 7.8 earthquake. To analyze the long-term movements of those IGS stations, we reference to results provided by Nevada Geodetic Laboratory. Daily GPS data are routinely processed at Nevada Geodetic Laboratory (Blewitt G. et al. 2018). According to their analysis, those IGS stations are moving at a long-term speed of less than 50 mm/yr, which makes it appropriate to assume the stations are relatively static in a few hours if they are not affected by seismic waves. We processed data from the station *sofi* with station *ista* as reference station and vice versa, through which we confirmed *sofi* with minor effects of the events and chose it as the reference station. The GPS data of other stations before seismic wave propagated to the station *sofi* is used in kinematic mode processing. Secondly, we use IGS final precise ephemeris of GPS constellation. Linear combinations of observations are used to eliminate first-order ionospheric

delay. The ionex files from Center for Orbit Determination in Europe (CODE) are used to estimate second order ionospheric delay. GPT3 model and VMF mapping functions are used for atmospheric delay estimation (re3data.org - Registry of Research Data Repositories. http://doi.org/10.17616/R3RD2H). Local coordinates of stations with continuous observations covering the Mw 7.8 event are obtained. The time series of 4 stations are shown in Fig. 2.

The accuracy of horizontal components of local coordinates of the stations is better than 2cm, which is appropriate to estimate displacements larger than several centimeters. The vertical components are less distinguishable for coseismic estimates, so only horizontal components are analyzed in this article.

Using least squares linear fitting, coseismic displacements are estimated as the difference between interceptions of fitting lines after and before the event. The estimated largest
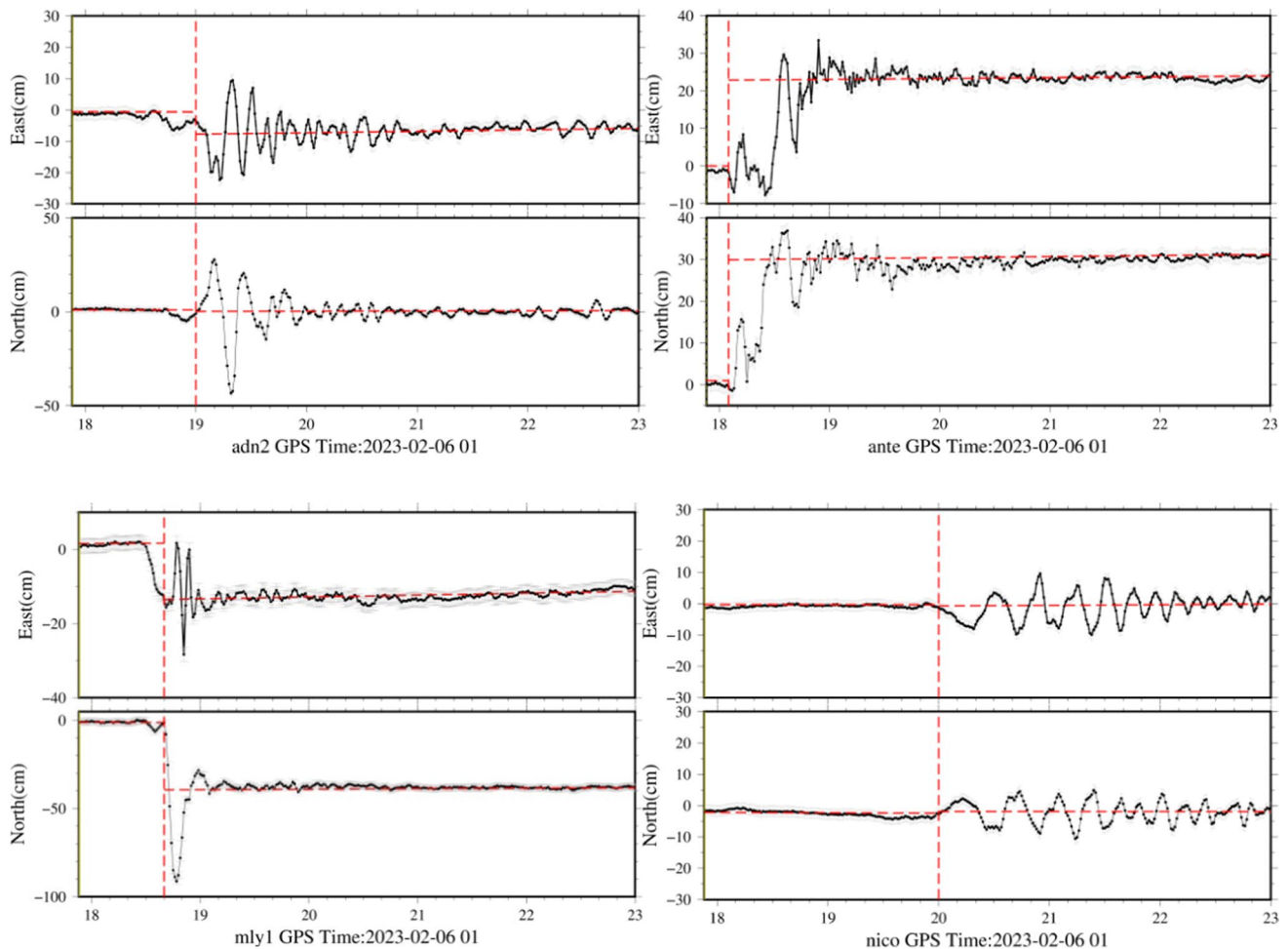

Fig. 2 Time series of the stations *adn2*(upper left), *ante*(upper right), *mly1*(lower left), *nico*(lower right) at GPS time 01on February 6,2023. In each panel, the positions of east (top) and north (bottom) components are shown with black dots for each second with grey error bars. X axis denotes GPS time, while Y axis denotes station position in centimeters. The X axis starts at the GPS time of the Mw 7.8 earthquake origin. Horizontal red dashed lines are least square fitting of time series before and after the event. Vertical red dashed lines denote the fitting time

displacements occurred are at station **ante** with an eastward component displacement of 31 cm and at station *mly1* with a southward component displacement of 39cm.

High-rate GPS time series analysis

As shown in Fig. 1, the focal mechanism for the Mw 7.8 event from GCMT gives one rupture nodal plane with a strike azimuth of 54° and a dip of 70° and the other with a strike azimuth of 320° and a dip of 80°. The focal mechanism for the Mw 7.5 event gives one rupture nodal plane with a strike azimuth of 261° and a dip of 42° and the other with a strike azimuth of 358° and a dip of 84°. To estimate the propagation speed of the surface wave radiated by the Mw 7.8 earthquake, three profiles are made along two nodal planes and eastward of the hypocenter as shown in Fig. 1. To simplify the processing, the middle time between the largest and smallest positions is defined as the average arrival time. Then each arrival time of the surface wave to the stations is obtained. The X axis is defined as the time measured in seconds after the event and the Y axis as the epicentral distance in kilometers, the time series are plotted in Fig. 3.

The overall estimation of surface wave propagation caused by the Mw 7.8 earthquake is at a speed of 2.983 km/s, while a speed of 3.135 Km/s at profile 1 in the NE direction, a speed of 3.101 km/s at profile 2 in the NW direction, and a speed of 3.055 km/s at profile 3 in the east direction.

Coseismic displacement estimates

Coseismic displacements at stations with continuous observations are estimated using time series that covers the Mw 7.8 event. However, 4 sites (*kls1*, *ekz1*, *akle*, and *vir2*) near the epicenter stopped recording data shortly after the event, possibly because of the severe shaking from the earthquake. The sites *kls1* and *vir2* stopped observation tens of seconds after the origin time and resumed observation at the nest hour, while the sites *ekz1* and *akle* stopped and resumed observation at one hour later. Data of one whole hour at GPS time 00 and 03 are processed and linearly fitted to the origin time of the Mw 7.8 event. Differences of the intercepts of the fitting lines at the origin time of the event are the displacement estimates accordingly.

To get consistent reference frames for the 4 stations, the Cartesian coordinates for the stations in ITRF 2014 are obtained for the two separated one-hour sessions. In order to use least squares linear fitting for the two sessions in the same reference frame, we concatenate the Cartesian coordinates of these two sessions of each station. Then the formulas 1, 2, and 3 are used to obtain local coordinates for each station, which leads to the north, east, and up component

coordinates relative to the first epoch local position at 0 o'clock of each station (Gerdan 1999). Thus the displacements of these stations in the consistent local coordinate system can be estimated using linear least squares estimation. To attest to the method, two stations (*ante* and *mly1*) with continuous observations through the Mw 7.8 earthquake are also processed. The estimations are shown in Fig. 4.

$$\begin{bmatrix} E \\ N \\ U \end{bmatrix} = \begin{bmatrix} -\sin B \cos L & -\sin B \sin L & \cos B \\ -\sin L & \cos L & 0 \\ \cos B \cos L & \cos B \sin L & \sin B \end{bmatrix} \begin{bmatrix} X - X_0 \\ Y - Y_0 \\ Z - Z_0 \end{bmatrix},$$

(1)

$$L = \arctan \frac{Y}{X},$$

(2)

$$B = \arctan \frac{Z}{(1-f)\sqrt{X^2 + Y^2}},$$

(3)

X_0, Y_0 and Z_0 are initial reference positions of local coordinates in the Cartesian coordinate system. B and L are geodetic latitude and longitude, and f is flattening of the ellipsoid.

The horizontal displacements of the two stations (*ante* and *mly1*) with continuous observations through the event are also estimated using this method and compared with linear fitting of continuous observations. Then the coseismic displacement distribution of all relevant stations is shown in Fig. 5.

The inferred displacements of these two stations (*ante* and *mly1*) show good consistency with direct estimates considering the centimeter level accuracy of the kinematic positioning. The north and east component differences at station *ante* are -3.8cm and 2.4cm, which is close to the positioning accuracy and less than 15% of total displacements. Furthermore, it should be noted that the method doesn't take other earthquakes into consideration, especially the Mw 6.7 earthquake (Fig. 1) which occurred close to the station *ante* and at the time shortly after the Mw 7.8 earthquake.

It can be seen from Fig. 5 that the stations in the northwest of the rupture moved southwest while the stations in the southeast moved northeast. The displacements decrease while the epicentral distances increase. The displacements caused by the event show left-lateral movement along the nodal plane, which is consistent with the GCMT focal mechanism. The estimated largest displacements occurred are at station *ante* with an eastward displacement of 31 cm and at station *mly1* with a southward displacement of 39 cm.

Using the same method, coseismic displacements of the stations caused by the Mw 7.5 earthquake are shown in Fig. 6. The largest component displacements caused by the Mw 7.5 event are a westward displacement of 450
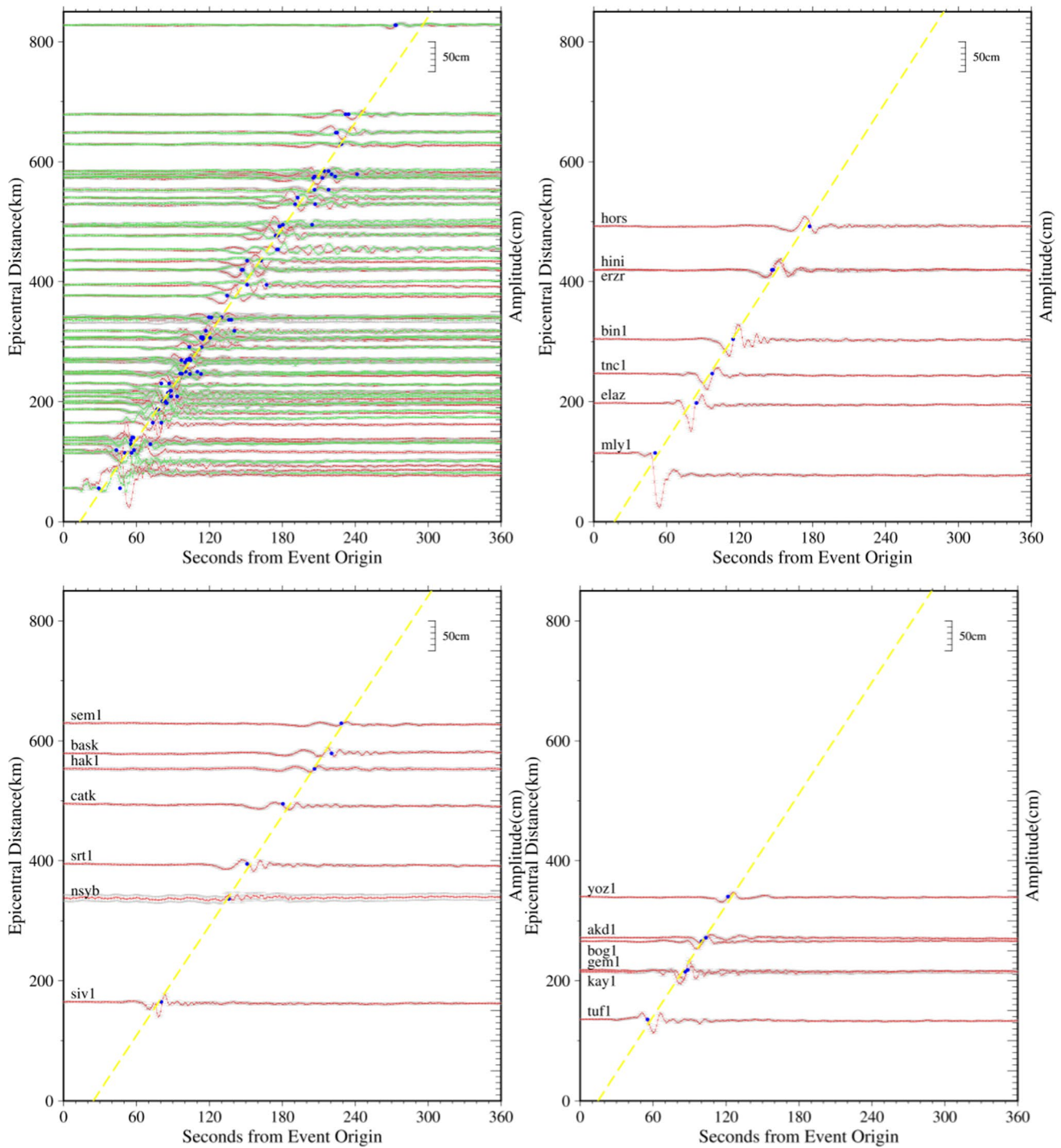
Fig. 3 Time series after the Mw 7.8 event. Upper-left panel for all stations. Upper-right panel is for profile 1 in Fig. 1. Lower-left panel is for profile 2. Lower-right panel is for profile 3. Red lines denote north component of time series while green lines denote east component. Blue dots denote average arrival times of stations. Yellow dashed lines are linear fitting to blue dots. X axis denotes seconds after the event. Y axis on the left denotes epicentral distances of the stations in kilometers, while Y axis on the right denotes position change with minimum tick interval indicating 10 centimeters

cm and a northward component displacement of 97 cm at the station *ekz1* which is only 6km from the epicenter of the event. The coseismic displacements to the east of the epicenter are mostly southward, while displacements to the west of the epicenter are mostly northward. The distribution
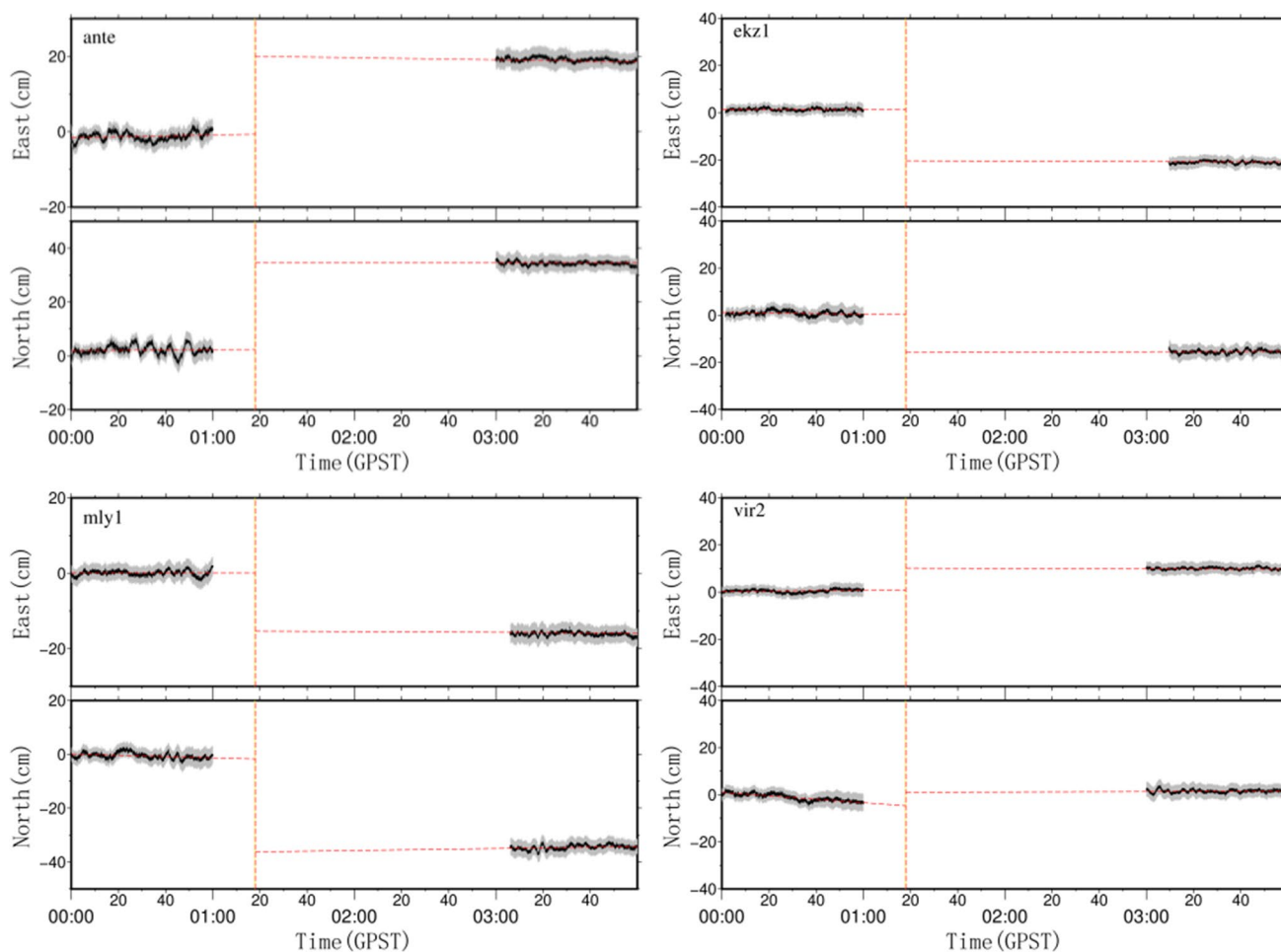
Fig. 4 Horizontal coseismic displacement estimates of *ante*, *ekz1*, *mly1*, and *vir2*. Horizontal red dashed lines are least squares fitting of time series before and after the event. Vertical red dashed lines denote the fitting time. Vertical yellow lines denote the origin time of the Mw 7.8 earthquake

of coseismic displacements is consistent with GCMT focal mechanism.

Discussions

The kinematic mode processing of high-rate GPS data provides an efficient method for coseismic displacement estimation, because only a short time of observations (several hours) is needed and it has a high temporal resolution to distinguish displacements caused by different earthquakes which occurred sequentially with a short interval. For the stations nearest to the epicenter which are severely affected by the earthquake, coseismic displacements could still be estimated with timely redeployed observations. It is critical that the reference station is static during the observation.

The background movement of the reference station is at a rather low speed to affect the position estimates during a few hours. Our method makes it possible to estimate

coseismic displacements shortly after an event with a prominent advantage of distinguishing seismic effects caused by each earthquake in one sequence which happened with short time intervals.

The linear fitting of time series could be made more plausible to estimate the start time of seismic waves of each station. With higher accuracy and higher sampling rate, it would effectively improve the estimation of surface wave propagation speed. The distribution of GPS stations at different epicentral distances would also contribute to better estimation. It should also be noted that post-seismic effects are ignored in this article because of short duration.

Using high-rate GPS observations, preliminary estimates of coseismic displacements and corresponding surface wave forms could be recorded with only a few hours of observations. The estimated largest displacements caused by the Mw 7.8 Pazarcik earthquake are observed at station *ante* with an eastward component displacement of 31 cm and at station *mly1* with a southward component displacement of
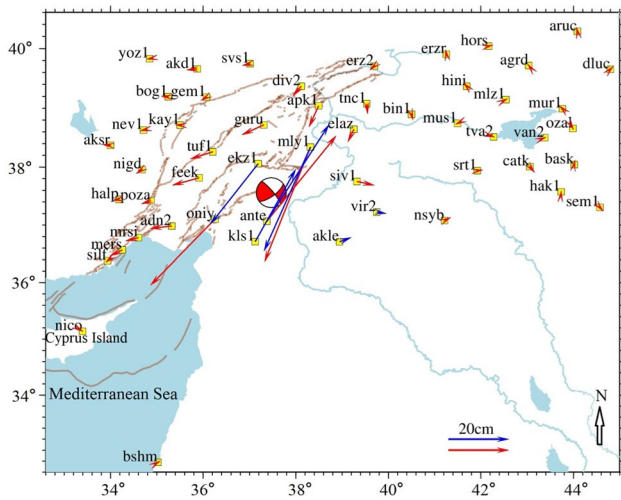
Fig. 5 Coseismic displacements of the stations caused by the Mw 7.8 event. Red arrows denote direct estimates of displacements from continuous high-rate GPS observation cover the Mw 7.8 event, blue ones denote estimates from 2 separate one-hour observations before and after the event
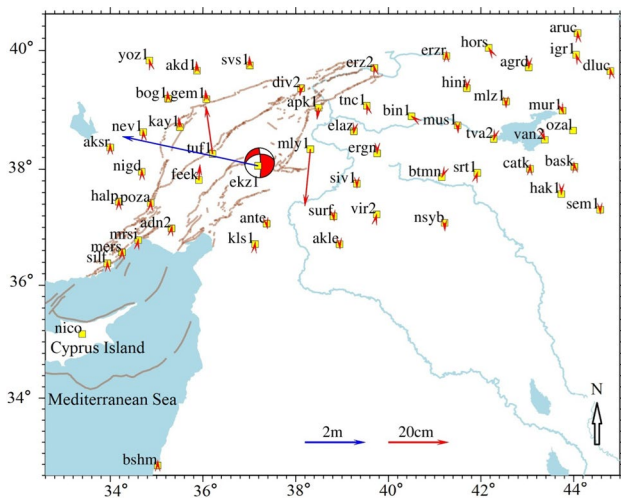

Fig. 6 Coseismic displacements of the stations caused by the Mw 7.5 event. Red arrows denote direct estimates of displacements from continuous high-rate GPS observations cover the Mw 7.5 event, the blue one at the station *ekz1* denote estimates from 2 separate one-hour observations before and after the event. The displacement of station *ekz1* is plotted with the blue scale which is different from the red ones. The displacement at station *ekz1* is over 4 meters

39 cm. The Mw 7.8 Pazarcik earthquake shows left-lateral movement along the nodal plane, which is consistent with the focal mechanism. The largest displacements caused by the Mw 7.5 Elbistan earthquake are a westward component displacement of 450 cm and a northward component displacement of 97 cm at the station *ekz1* which is about 6 km from the epicenter of the event. Based on high-rate GPS time series, the surface wave propagation of the Mw 7.8

Elbistan earthquake is preliminarily estimated at an overall speed of approximately 2.9 km/s. High-rate GPS observations show prominent advantage of temporal resolution for earthquake sequences with short intervals. The displacement estimation provides constraints for inversion of the rupture process and seismic source mechanism. Daily observations provide another way of estimation of coseismic displacements. Comparisons between these two methods are relevant to observation time and models, which is beyond the scope of this article. As a prominent advantage of high-rate GPS observations for coseismic displacements are the rapid estimations and further applications for geophysical purposes.

With shorter observation time, the coseismic displacement estimations of different earthquakes could be available for higher temporal resolution, while other geodetic observations with longer interval could only provide the comprehensive displacements of earthquakes. The linear fitting of position time series of high-rate GPS observations is meaningful only for sites with displacements large enough to be distinguished from noise, so more accurate observations will prompt coseismic displacement estimations. And other earthquakes such as the Mw 6.7 event would be distinguished from position time series with closest sites within tens of kilometers. Additionally, spatially uniform distributed sites will provide more information on surface wave propagation speed, especially sites at different epicentral distances will provide constraints for different locations.

Author contributions FS and LJ designed the study. FS developed data processing method. LG collected the data and implemented linear fitting. LR performed the analyses for IGS stations. AK prepared the figures. SY executed the calculations and FS drafted the manuscript. All authors interpreted the results and provided input to the analysis and manuscript.

Data availability All data products utilized in this analysis are in the public domain. Links to their sources are provided in the text.

Declarations

Conflict of interest The authors declare that they have no conflicts of interest.

References

Abdrakhmatov K. Ye., Aldazhanov SA et al. (1996) Relatively recent construction of the Tien Shan inferred from GPS measurements of present-day crustal deformation rates. Nature 384:450–453. https://doi.org/10.1038/384450a0

Avallone A et al. (2012) High-rate (1 Hz to 20 Hz) GPS coseismic dynamic displacements carried out during the Emilia 2012 seismic sequence. Ann Geophys. https://doi.org/10.4401/ag-6162

Barka AA, Reilinger R (1997) Active tectonics of the Mediterranean region: deduced from GPS, neotectonic and seismicity data. Ann Geofisica 40:587–610

Blewitt G, Kreemer C et al (2006) Rapid determination of earthquake magnitude using GPS for tsunami warning systems. Geophys Res Lett 33:L11309. https://doi.org/10.1029/2006GL026145

Blewitt G, Hammond WC, Kreemer C (2018) Harnessing the GPS data explosion for interdisciplinary science. Eos. https://doi.org/10.1029/2018EO104623

Bulut F, Bohnhoff M, Eken T, Janssen C, Kılıç T, Dresen G (2012) The east anatolian fault zone: seismotectonic setting and spatiotemporal characteristics of seismicity based on precise earthquake locations. J Geophys Res 117:B07304. https://doi.org/10.1029/2011JB008966

Ekström G, Nettles M, Dziewoński AM (2012) The global CMT project 2004–2010: Centroid-moment tensors for 13,017 earthquakes. Phys Earth Planetary Interiors 200–201:1–9. https://doi.org/10.1016/j.pepi.2012.04.002

Elósegui P, Davis JL, Oberlander D et al (2006) Accuracy of high-rate GPS for seismology. Geophys Res Lett 33(11):L11308

Emre Ö, Duman TY, Özalp S et al (2018) Active fault database of Turkey. Bull Earthq Eng 16:3229–3275. https://doi.org/10.1007/s10518-016-0041-2

Ge L, Han S, Rizos C et al (2000) GPS seismometers with up to 20-Hz sampling rate. Earth Planets Space 52(10):881–884

Gerdan GP, Deakin RE (1999) Transforming cartesian coordinates X, Y, Z to geographical coordinates φ, λ, h. Australian Surveyor 44(1):55–63. https://doi.org/10.1080/00050351.1999.10558773

Goldberg DE, Melgar D, Bock Y, Allen RM (2018) Geodetic observations of weak determinism in rupture evolution of large earthquakes. J Geophys Res Solid Earth 123:9950–9962. https://doi.org/10.1029/2018JB015962

Goudarzi MA, Cocard M, Santerre R (2016) Present-day 3d velocity field of eastern north America based on continuous gps observations. Pure Appl Geophys 173(7):2387–2412

Guo B, Di M, Song F et al (2021) Integrated coseismic displacement derived from high-rate GPS and Strong-motion seismograph: application to the 2017 Ms 7.0 Jiuzhaigou Earthquake. Measurement 182(2):109735

Herring T. A. (2003) GLOBK: Global Kalman filter VLBI and GPS analysis program Version 10.1 Internal Memorandum, Massachusetts Institute of Technology, Cambridge.

Jia Zhijie, Peng Jianbing, Quanzhong Lu et al (2022) Formation mechanism of ground fissures originated from the hanging wall of normal fault: a case in Fen-Wei Basin China. J Earth Sci 33(2):482–492. https://doi.org/10.1007/s12583-021-1508-x

Jiang Z et al (2014) GPS constrained coseismic source and slip distribution of the 2013 Mw6.6 Lushan, China, earth-quake and its tectonic implications. Geophys Res Lett 41:407–413. https://doi.org/10.1002/2013GL05881

Larson K (2009) GPS seismology. J Geodesy 83(3):227–233

Larson K, Bodin P, Gomberg J (2003) Using 1-Hz GPS data to measure deformations caused by the Denali fault earthquake. Science 300:1421–1424

Li Q, You XZ, Yang SM, Du RL, Qiao XJ, Wang Q (2012) A precise velocity field of tectonic deformation in China as inferred from intensive GPS observations. Sci China Ser D 55:695–698. https://doi.org/10.1007/s11430-012-4412-5

Li J, Yao Y, Li R, Yusan S, Li G, Freymuller JT, Wang Q (2022) Present-day strike-slip faulting and thrusting of the Kepingtage fold-and-thrust belt in southern Tianshan: constraints from GPS observations. Geophys Res Lett 49:e2022GL099105

Li X, Chen C, Liang H et al (2023) Earthquake source parameters estimated from high-rate multi-GNSS data: a case study of the 2022 M6.9 Menyuan earthquake. Acta Geophys 71(2):625–636

McKenzie Dan (1972) Active tectonics of the mediterranean region. Geophys J Royal Astron Soc 1972(30):109–185

Melgar D, Bock Y, Crowell BW (2012) Real-time centroid moment tensor determination for large earthquakes from local and regional displacement records. Geophys J Int 188:703–718. https://doi.org/10.1111/j.1365-246X.2011.05297.x

Michel C, Kelevitz K et al (2017) The potential of high-rate GPS for strong ground motion ssessment. Bull Seismol Soc Am 107(4):1849–1859. https://doi.org/10.1785/0120160296

Noll CE (2010) The crustal dynamics data information system: a resource to support scientific analysis using space geodesy. Adv Space Res 45(12):1421–1440

Reitman, Nadine G et al (2023) Preliminary fault rupture mapping of the 2023 M7.8 and M7.5 Türkiye Earthquakes. https://doi.org/10.5066/P985I7U2

Seyitoğlu G, Tunçel E et al (2022) The Anatolian diagonal: a broad left-lateral shear zone between the north anatolian fault zone and the aegean/cyprus arcs. Türkiye Jeoloji Bülteni 65(2):93–116. https://doi.org/10.25288/tjb.1015537

Wu Y, Jiang Z, Pang Y et al (2022) Statistical correlation of seismicity and geodetic strain rate in the Chinese Mainland. Seismol Res Lett 1:93

Xu P, Du F, Shu Y et al (2021) Regularized reconstruction of peak ground velocity and acceleration from very high-rate GNSS precise point positioning with applications to the 2013 Lushan Mw6.6 earthquake. J Geod 95:17. https://doi.org/10.1007/s00190-020-01449-6

Yokota Y, Koketsu K, Hikima K, Miyazaki S (2009) Ability of 1-Hz GPS data to infer the source process of a medium-sized earthquake: the case of the 2008 Iwate-Miyagi Nairiku, Japan, earthquake. Geophys Res Lett. https://doi.org/10.1029/2009GL037799

Yue H, Lay T (2011) Inversion of high-rate (1 sps) GPS data for rupture process of the 11 March 2011 Tohoku earthquake (Mw 9.1). Geophys Res Lett. https://doi.org/10.1029/2011GL048700

Yuji Itoh, Yosuke Aoki, Junichi Fukuda (2022) Imaging evolution of Cascadia slow-slip event using high-rate GPS. Sci Rep 12:7179. https://doi.org/10.1038/s41598-022-10957-8

Zhan W, Heki K, Arief S, Yoshida M (2021) Topographic amplification of crustal subsidence by the rainwater load of the 2019 typhoon Hagibis in Japan. J Geophys Res: Solid Earth 126:e2021JB021845. https://doi.org/10.1029/2021JB021845